

See discussions, stats, and author profiles for this publication at: <https://www.researchgate.net/publication/42805527>

Ultrathin n-Type Organic Nanoribbons with High Photoconductivity and Application in Optoelectronic Vapor Sensing of Explosives

ARTICLE *in* JOURNAL OF THE AMERICAN CHEMICAL SOCIETY · MARCH 2010

Impact Factor: 12.11 · DOI: 10.1021/ja909797q · Source: PubMed

CITATIONS

120

READS

59

8 AUTHORS, INCLUDING:



Xiaomei Yang

University of Utah

33 PUBLICATIONS 1,855 CITATIONS

SEE PROFILE

Ultrathin n-Type Organic Nanoribbons with High Photoconductivity and Application in Optoelectronic Vapor Sensing of Explosives

Yanke Che,[†] Xiaomei Yang,[†] Guilin Liu,[‡] Chun Yu,[‡] Hongwei Ji,[‡] Jianmin Zuo,[§]
Jincai Zhao,^{*,‡} and Ling Zang^{*,†}

Department of Materials Science and Engineering, University of Utah, Salt Lake City, Utah 84108, Key Laboratory of Photochemistry, Institute of Chemistry, Chinese Academy of Sciences, Beijing 100080, People's Republic of China, and Departments of Materials Science and Engineering, University of Illinois at Urbana–Champaign, Urbana, Illinois 61801

Received November 30, 2009; E-mail: jczhao@iccas.ac.cn; lzang@eng.utah.edu

Abstract: Well-defined ultrathin nanoribbons have been fabricated from an amphiphilic electron donor–acceptor (D–A) supramolecule comprising perylene tetracarboxylic diimide as the backbone scaffold to enforce the one-dimensional intermolecular assembly via strong π -stacking. These nanoribbons demonstrated high photoconductivity upon illumination with white light. The high photoconductivity thus obtained is likely due to the optimal molecular design that enables a good kinetic balance between the two competitive processes, the intramolecular charge recombination (between D and A) and the intermolecular charge transport along the nanoribbon. The photoconduction response has also proven to be prompt and reproducible with the light turning on and off. The photogenerated electrons within the nanoribbon can be efficiently trapped by the adsorbed oxygen molecules or other oxidizing species, leading to depletion of the charge carriers (and thus the electrical conductivity) of the nanoribbon, as typically observed for n-type semiconductor materials as applied in chemiresistors. Combination of this sensitive modulation of conductivity with the unique features intrinsic to the nanoribbon morphology (large surface area and continuous nanoporosity when deposited on a substrate to form a fibril film) enables efficient vapor sensing of nitro-based explosives.

Introduction

One-dimensional (1D) nanostructures represent attractive building blocks for nanoscale optoelectronic devices.^{1–5} Among these 1D nanostructures, photoconductive materials have drawn intensive interest for their applications in photodetectors,^{6–9} optical switches,^{2,10–13} and sensors.^{2,14–16} To date, most of these

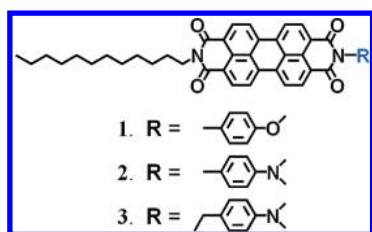
nanodevices are fabricated from inorganic nanowires^{2,6–8,14–16} and carbon nanotubes,¹⁷ whereas only a few such photoconductive 1D nanostructures have been reported on organic materials,^{10–12,18} despite their various advantages over their inorganic counterparts including chemically tunable electronic and optical properties and conformal flexibility and adaptability. Moreover, among the limited number of 1D organic nanomaterials that demonstrated a photoconductivity response, most of them were a p-type semiconductor, i.e., hole acting as the transporting charge carrier. This is partially due to the limited availability of air-stable n-type organic materials.^{19,20}

One way to approach high photoconductivity is to fabricate the 1D nanomaterials from building-block molecules that contain covalently linked electron donor (D) and acceptor (A) units,

- [†] University of Utah.
[‡] Chinese Academy of Sciences.
[§] University of Illinois at Urbana–Champaign.
(1) Hoebe, F. J. M.; Jonkheijm, P.; Meijer, E. W.; Schenning, A. P. H. J. *Chem. Rev.* **2005**, *105*, 1491–1546.
(2) Xia, Y.; Yang, P.; Sun, Y.; Wu, Y.; Mayers, B.; Gates, B.; Yin, Y.; Kim, F.; Yan, H. *Adv. Mater.* **2003**, *15*, 353–389.
(3) Hu, J.; Odom, T. W.; Lieber, C. M. *Acc. Chem. Res.* **1999**, *32*, 435–445.
(4) Zang, L.; Che, Y.; Moore, J. S. *Acc. Chem. Res.* **2008**, *41*, 1596–1608.
(5) Zhao, Y. S.; Fu, H.; Peng, A.; Ma, Y.; Xiao, D.; Yao, J. *Adv. Mater.* **2008**, *20*, 2859–2876.
(6) Wang, J.; Gudiksen, M. S.; Duan, X.; Cui, Y.; Lieber, C. M. *Science* **2001**, *293*, 1455–1457.
(7) Kind, H.; Yan, H.; Messer, B.; Law, M.; Yang, P. *Adv. Mater.* **2002**, *14*, 158–60.
(8) Ahn, Y.; Dunning, J.; Park, J. *Nano Lett.* **2005**, *5*, 1367–1370.
(9) O'Brien, G. A.; Quinn, A. J.; Tanner, D. A.; Redmond, G. *Adv. Mater.* **2006**, *18*, 2379–2383.
(10) Yamamoto, Y.; Fukushima, T.; Suna, Y.; Ishii, N.; Saeki, A.; Seki, S.; Tagawa, S.; Taniguchi, M.; Kawai, T.; Aida, T. *Science* **2006**, *314*, 1761–1764.
(11) Schwab, A. D.; Smith, D. E.; Bond-Watts, B.; Johnston, D. E.; Hone, J.; Johnson, A. T.; dePaula, J. C.; Smith, W. F. *Nano Lett.* **2004**, *4*, 1261–1265.

- (12) Jiang, L.; Fu, Y.; Li, H.; Hu, W. *J. Am. Chem. Soc.* **2008**, *130*, 3937.
(13) Zhang, Y.; Chen, P.; Jiang, L.; Hu, W.; Liu, M. *J. Am. Chem. Soc.* **2009**, *131*, 2756–2757.
(14) Gong, J.; Li, Y.; Chai, X.; Hu, Z.; Deng, Y. *J. Phys. Chem. C*, **114**, 1293–1298.
(15) Lao, C.; Li, Y.; Wong, C. P.; Wang, Z. L. *Nano Lett.* **2007**, *7*, 1323–1328.
(16) Wang, D.; Hao, C.; Zheng, W.; Peng, Q.; Wang, T.; Liao, Z.; Yu, D.; Li, Y. *Adv. Mater.* **2008**, *20*, 2628–2632.
(17) Freitag, M.; Martin, Y.; Misewich, J. A.; Martel, R.; Avouris, P. *Nano Lett.* **2003**, *3*, 1067–71.
(18) Zhang, X.; Jie, J.; Zhang, W.; Zhang, C.; Luo, L.; He, Z.; Zhang, X.; Zhang, W.; Lee, C.; Lee, S. *Adv. Mater.* **2008**, *20*, 2427–2432.
(19) Newman, C. R.; Frisbie, C. D.; da Silva Filho, D. A.; Bredas, J.-L.; Ewbank, P. C.; Mann, K. R. *Chem. Mater.* **2004**, *16*, 4436–4451.
(20) Jones, B. A.; Facchetti, A.; Wasielewski, M. R.; Marks, T. J. *J. Am. Chem. Soc.* **2007**, *129*, 15259–15278.

Chart 1



for which efficient charge separation can be initiated upon photoexcitation.¹⁰ However, assembling the covalently linked D/A molecules into continuous 1D stacks remains challenging, as the strong charge transfer interaction between the D/A moieties often causes them to stack on each other,^{21,22} producing a bulk mixed phase, where the rapid charge recombination between D^+ and A^- dominates the loss of photogenerated charge carriers. While instant photoinduced charge separation can be achieved for many D/A systems, the subsequent long-range intermolecular charge transport (toward the electrodes) is often a bottleneck for approaching high efficiency of photocurrent generation. To date, only a few D/A molecules have successfully been fabricated into segregated, highly organized 1D nanostructures that afford high photoconductivity.^{10,23}

Herein we report the fabrication of well-defined ultrathin nanoribbons from the D/A molecules based on the scaffold of perylene tetracarboxylic diimide (PTCDI, Chart 1), which forms a class of n-type semiconductor materials with strong electron affinity (particularly in the photoexcited state).^{19,24} The extended 1D intermolecular arrangement (dominated by the cofacial π – π stacking of PTCDI scaffolds) is expected to be conducive to charge transport along the nanoribbon, leading to highly efficient photocurrent generation, as indeed observed in this study. Among the three building-block molecules employed in this study, molecule **1** (without D moiety) is selected as a reference to prove the mechanism of photocurrent generation, i.e., originated via photoinduced intramolecular charge separation between the D and A moiety, while molecules **2** and **3** are selected for comparative investigation, aiming to further explore how to enhance the photocurrent generation through controlling the intramolecular charge separation to match the subsequent intermolecular charge transport along the π – π stack.

Although photoinduced charge transfer has been well exploited for many PTCDI-based D/A molecules and their aggregates in solution,^{25–29} only a few of these molecular systems have been fabricated into well-defined 1D nanostructures,

and none of the 1D nanostructures thus fabricated demonstrated significant photoconductivity. The high photoconductivity obtained in this study for the PTCDI nanoribbons enables potential application in vapor sensing of oxidizing species. Surface adsorption of these electron-withdrawing species will decrease the charge carrier density within the nanoribbon through surface trapping of the electrons, resulting in a decrease in electrical conductivity in a manner similar to that operating in a chemiresistor or chemical-field-effect transistor.^{30,31} Indeed, as described below, a dramatic decrease in photoconductivity was observed for the PTCDI nanoribbons when exposed to oxygen or other oxidizing species including nitro-based explosives. Sensor development along this line will take advantage of the ultrathin nanoribbon morphology, which offers enlarged surface area and thus strong surface adsorption of gaseous species.

Results and Discussion

Synthesis of Molecules and Self-Assembly into Nanoribbons. The molecular design and synthesis take advantage of the fact that the two nitrogen positions in PTCDI are nodes in the π -orbitals,^{4,24,32} and thus the side-chain substitution does not affect the electronic properties (particularly the electron affinity) of the PTCDI backbone. This unique feature offers enormous options for side-chain modification of PTCDI, producing candidate molecules suited not only for the 1D assembly into nanoribbon structure but also for comparative investigation of the intramolecular charge separation depending on the D–A linkage and the effect on the overall photocurrent generation within the nanoribbon. The three PTCDI molecules (**1–3**) linked to different functional moieties (as shown in Chart 1) are selected for this comparative investigation, for which the *N,N*-dimethylaniline moiety acts as a strong electron donor to yield the photoinduced charge separation with the PTCDI unit, while the methoxyphenyl moiety is redox inert and employed for comparison purposes (Figure S1). Efficient intramolecular photoinduced electron transfer (fluorescence quenching) was previously observed for the PTCDI molecules directly linked with an aniline moiety.³³ Molecules **1–3** were synthesized from the perylene monoimide and corresponding amines following the procedure previously developed in our lab and others (see Experimental Section).^{4,34}

Considering the fact that 1D molecular assembly of the PTCDI-based molecules is usually dominated by the π – π interaction between the large perylene planes (in cooperation with the hydrophobic interactions between the long alkyl side chains),⁴ the three building-block molecules are expected to produce similar intermolecular arrangement and thus approximately the same size and morphology of the final assembled materials, specifically nanoribbons, as indeed revealed by the SEM and AFM imaging shown in Figure 1. The fabrication of the nanoribbons was performed through solution-based self-assembly following a protocol similar to that previ-

- (21) Pisula, W.; Kastler, M.; Wasserfallen, D.; Robertson Joseph, W. F.; Nolde, F.; Kohl, C.; Mullen, K. *Angew. Chem., Int. Ed.* **2006**, *45*, 819–23.
- (22) Percec, V.; Glodde, M.; Bera, T. k.; Miura, Y.; Shiyonovsaya, I.; Singer, K. D.; Balagurusamy, V. S. K.; Helney, P. A.; Schnell, I.; Rapp, A.; Spiess, H. W.; Hudson, S. D.; Duan, H. *Nature* **2002**, *417*, 384–387.
- (23) Kishore, R. S. K.; Kel, O.; Banerji, N.; Emery, D.; Bollot, G.; Mareda, J.; Gomez-Casado, A.; Jonkheijm, P.; Huskens, J.; Maroni, P.; Borkovec, M.; Vauthey, E.; Sakai, N.; Matile, S. *J. Am. Chem. Soc.* **2009**, *131*, 11106–11116.
- (24) Wurthner, F. *Chem. Commun.* **2004**, 1564–79.
- (25) Schenning, A. P. H. J.; Herrikhuyzen, J. V.; Jonkheijm, P.; Chen, Z.; Wurthner, F.; Meijer, E. W. *J. Am. Chem. Soc.* **2002**, *124*, 10252–10253.
- (26) Wurthner, F.; Chen, Z.; Hoebe, F. J. M.; Osswald, P.; You, C. C.; Jonkheijm, P.; Herrikhuyzen, J. v.; Schenning, A. P. H. J.; vander Schoot, P. P. A. M.; Meijer, E. W.; Beckers, E. H. A.; Meskers, S. C. J.; Janssen, R. A. J. *J. Am. Chem. Soc.* **2004**, *126*, 10611–10618.
- (27) Beckers, E. H. A.; Meskers, S. C. J.; Schenning, A. P. H. J.; Chen, Z.; Wurthner, F.; Marsal, P.; Beljonne, D.; Cornil, J.; Janssen, R. A. J. *J. Am. Chem. Soc.* **2005**, *128*, 649.

- (28) Bullock, J. E.; Carmieli, R.; Mickley, S. M.; Vura-Weis, J.; Wasielewski, M. R. *J. Am. Chem. Soc.* **2009**, *131*, 11919.
- (29) Kelley, R. F.; Shin, W. S.; Rybtchinski, B.; Sinks, L. E.; Wasielewski, M. R. *J. Am. Chem. Soc.* **2007**, *129*, 3173.
- (30) Xie, D.; Jiang, Y.; Pan, W.; Jiang, J.; Wu, Z.; Li, Y. *Thin Solid Films* **2002**, *406*, 262–267.
- (31) Antonisse, M. M. G.; Snellink-Ruel, B. H. M.; Yigit, I.; Engbersen, J. F. J.; Reinhoudt, D. N. *J. Org. Chem.* **1997**, *62*, 9034.
- (32) Kazmaier, P. M.; Hoffmann, R. *J. Am. Chem. Soc.* **1994**, *116*, 9684–91.
- (33) Zang, L.; Liu, R.; Holman, M. W.; Nguyen, K. T.; Adams, D. M. *J. Am. Chem. Soc.* **2002**, *124*, 10640–10641.
- (34) Langhals, H. *Heterocycles* **1995**, *40*, 477–500.

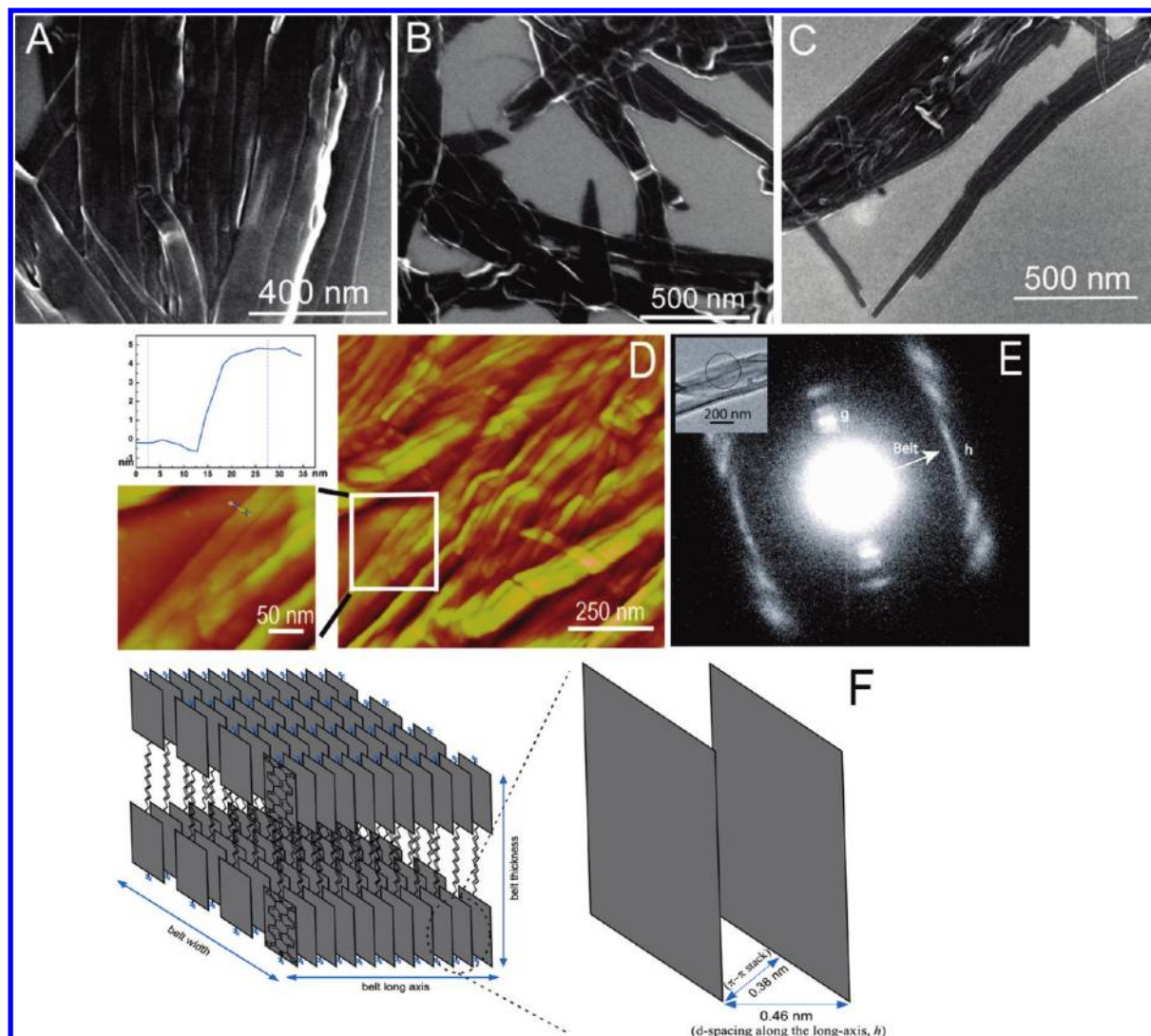


Figure 1. (A–C) SEM images showing the nanoribbons fabricated from molecules **3**, **2**, and **1**, respectively; (D) AFM image of the nanoribbons of molecule **3**; (E) electron-diffraction pattern recorded over a single nanoribbon cast on carbon film; (F) schematic diagram showing the intermolecular arrangement within the nanoribbon.

ously developed in our lab (see Experimental Section). The amphiphilic character of the three molecules is highly favorable for self-assembly through π – π stacking in hydrophilic solvents such as ethanol, where the hydrophilic part tends to stretch out into the solvent, while the hydrophobic alkyl side chains tend to interdigitate one another to hold the PTCDI scaffolds together, thus facilitating the 1D π – π stacking growth.^{10,35,36} The nanoribbons thus fabricated are several micrometers long (Figure S4) and a few tens of nanometers wide. The ribbon morphology was clearly revealed by AFM imaging and line scanning (Figure 1D and Figure S2), which indicates a thickness of only about 5 nm for all the nanoribbons under investigation. This thickness corresponds to the length of the two layers of PTCDI molecules tail-to-tail interdigitated, which finally constitutes the ribbon construction as schematically depicted in Figure 1F. Such a layered structure as controlled by the strong interdigitation between the alkyl side chains was previously observed for self-assembly of other amphiphilic molecules into ribbon-like

nanostructures.³⁷ Upon growth into even larger sizes, the 1D assembly obtained from molecule **1** still maintained the ribbon morphology (as shown in Figure S3), which is likely due to the layered intermolecular arrangement.

XRD measurement over the nanoribbons gave multiple distinct diffraction peaks (Figure S5). The whole spectrum is dominated by a single sharp peak at $2\theta = 3.98$, typically characteristic of a columnar stacked phase.³⁸ The d -spacing of 2.2 nm as deduced from this peak corresponds to the inter-columnar distance, i.e., about half of the length of two PTCDI molecules tail-to-tail interdigitated (Figure 1F), as indeed measured by AFM for the thickness of the nanoribbons (Figure 1D and Figure S2). The d -spacing corresponding to the cofacial intermolecular stacking is also observed at 0.38 nm, which is consistent with the π – π stacking distance usually observed for the stacking between planar aromatic molecules. To further determine the intermolecular organization within the nanoribbons, electron diffraction was performed over single nanorib-

(35) Che, Y.; Datar, A.; Balakrishnan, K.; Zang, L. *J. Am. Chem. Soc.* **2007**, *129*, 7234–7235.

(36) Palmer, L. C.; Stupp, S. I. *Acc. Chem. Res.* **2008**, *41*, 1674.

(37) Zubarev, E. R.; Sone, E. D.; Stupp, S. I. *Chem.–Eur. J.* **2006**, *12*, 7313–7327.

(38) Bushey, M. L.; Hwang, A.; Stephens, P. W.; Nuckolls, C. *J. Am. Chem. Soc.* **2001**, *123*, 8157–8.

bons, and one such pattern is shown in Figure 1E, where the two perpendicular reflections are labeled as g and h . h is parallel to the ribbon, while g is normal to the long axis of the ribbon. These two reflections give d -spacings of 0.46 and 0.74 nm, respectively, which are consistent with the XRD results. The d -spacing of 0.46 nm is due to the edge-to-edge (center-to-center) distance between the tiltedly stacked PTCDI planes (Figure 1F). Such tilted stacking is often observed for molecular crystals to minimize the free energy caused by the electronic repulsion.³² The strong π - π interaction is also consistent with the formation of a new, pronounced absorption band centered at 585 nm as measured for the nanoribbons in comparison to the molecular solutions (Figure S6A).^{24,39} The isosbestic point at 544 nm confirms a stoichiometric conversion from free molecules to crystal phase. All these experimental observations are supportive of the molecular arrangement as depicted in Figure 1F. The similar bilayer configuration is also reminiscent of the intermolecular arrangement reported for other amphiphilic molecules.^{10,37,40,41}

Photoconductivity of the Assembled Nanoribbons. The 1D molecular arrangement shown in Figure 1 is expected to give rise to efficient charge transport via the strong π -electron delocalization as previously evidenced by both theoretical and experimental observation.^{42–46} As shown in Figure 2A, the nanoribbons fabricated from molecule **3** indeed demonstrated very high photoconductivity upon irradiation with white light, whereas in the dark the same nanoribbons were hardly conductive, showing current in the range of pA. At an applied bias of 10 V, electrical current in the range of nA was obtained even under a low power irradiation, e.g., 0.3 mW/mm², producing a photocurrent on/off ratio of ca. 10³. This value is expected to be much larger if higher power irradiation and/or longer electrode pairs were employed for the photocurrent measurement.⁴⁷ The photoconduction switching has also proven to be prompt and reproducible with the light turning on and off (Figure 2B), implying not only fast photoresponse but also the high stability of the materials when operated under ambient conditions.

The same geometry and similar size obtained for the nanoribbons fabricated from the three molecules provide rationale for the comparative study of the photocurrent response. As a control, the nanoribbons fabricated from **1** demonstrated negligible photocurrent response (with an on/off ratio of only ca. 4), mainly because of the fact that there is no photoinduced

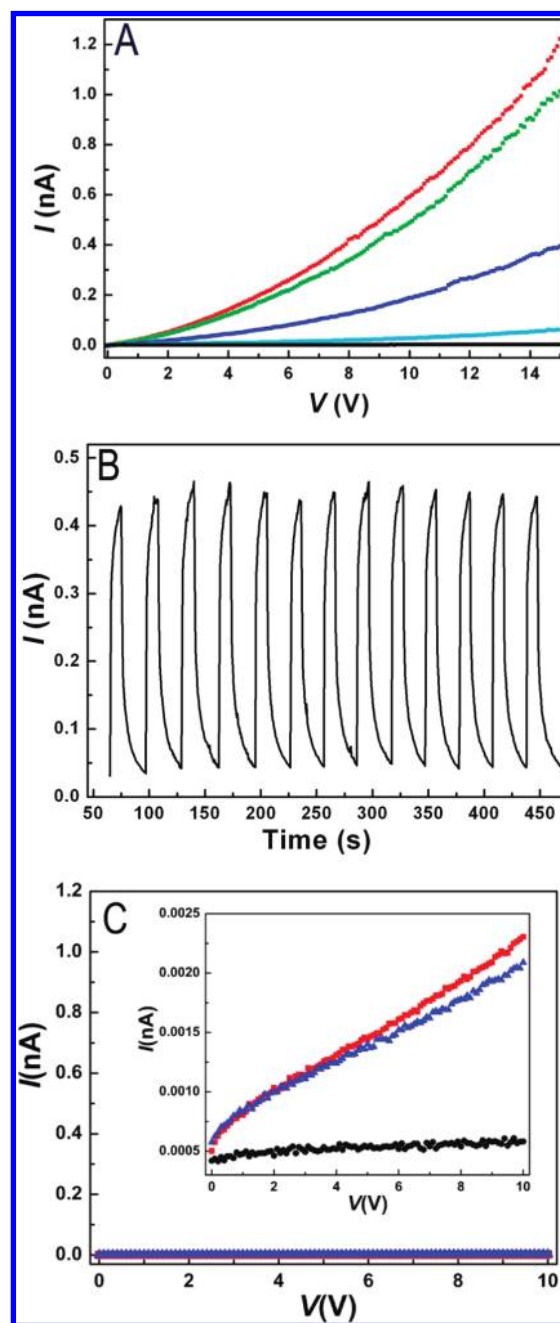


Figure 2. (A) I - V curves measured over the nanoribbons of **3** in the dark (black) and under white light irradiation of increasing power density (cyan: 0.005, blue: 0.03, green: 0.25, red: 0.3 mW/mm²); (B) photocurrent (at 10 V) in response to turning on and off the irradiation (0.3 mW/mm²); (C) I - V curves for the nanoribbons of **1** (red) and **2** (blue) under white light irradiation of power density 0.3 mW/mm² and in the dark (black). Inset: the same plots in zoom-in scale. Electrode pair: 3 μ m gap, 14 μ m long.

charge separation within this molecule (Figure S1). The lack of intramolecular charge separation is also consistent with the strong fluorescence emission observed for the nanoribbons fabricated from this molecule (Figure S7B). In contrast, both molecules **2** and **3** contain an aniline moiety as the electron donor, enabling efficient photoinduced intramolecular electron transfer (with a driving force as large as 1.1 eV, Figure S1). As a result, no fluorescence emission (due to complete quenching) was observed for the nanoribbons fabricated from these two molecules (Figure S7D,F). On the other hand, the strong fluorescence of molecules **2** and **3** can be restored simply by

- (39) Che, Y.; Yang, X.; Loser, S.; Zang, L. *Nano Lett.* **2008**, *8*, 2219–2223.
- (40) Zhang, X.; Chen, Z.; Wurthner, F. *J. Am. Chem. Soc.* **2007**, *129*, 4886–4887.
- (41) Yang, W.-Y.; Lee, E.; Lee, M. *J. Am. Chem. Soc.* **2006**, *128*, 3484.
- (42) Crispin, X.; Cornil, J.; Friedlein, R.; Okudaira, K. K.; Lemaire, V.; Crispin, A.; Kestemont, G.; Lehmann, M.; Fahlman, M.; Lazzaroni, R.; Geerts, Y.; Wendin, G.; Ueno, N.; Bredas, J.-L.; Salaneck, W. R. *J. Am. Chem. Soc.* **2004**, *126*, 11889–11899.
- (43) Cohen, Y. S.; Xiao, S.; Steigerwald, M. L.; Nuckolls, C.; Kagan, C. R. *Nano Lett.* **2006**, *6*, 2838–2841.
- (44) Rochefort, A.; Martel, R.; Avouris, P. *Nano Lett.* **2002**, *2*, 877–880.
- (45) Sofos, M.; Goldberger, J.; Stone, D. A.; Allen, J. E.; Ma, Q.; Herman, D. J.; Tsai, W.-W.; Lauhon, L. J.; Stupp, S. I. *Nat. Mater.* **2009**, *8*, 68–75.
- (46) Messmore, B. W.; Hulvat, J. F.; Sone, E. D.; Stupp, S. I. *J. Am. Chem. Soc.* **2004**, *126*, 14452.
- (47) Due to the negligible conductivity of the materials in the dark, depositing more materials within the two-electrode junction will bring little change to the dark current. However, the photocurrent will increase proportionally with the amount of materials deposited. Therefore, the longer the electrode used, the more materials incorporated, and thus the higher the on/off ratio obtained, as previously practiced by Aida et al.¹⁰

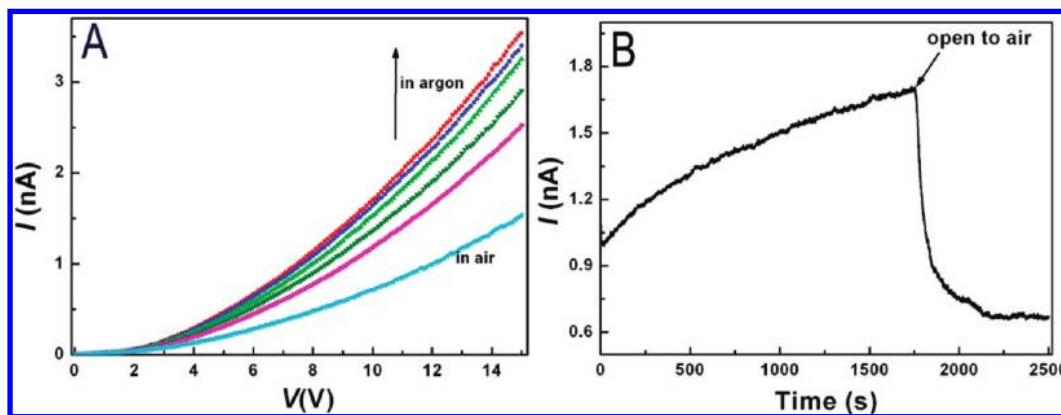


Figure 3. (A) I - V curves measured over the nanoribbons of **3** in air (cyan) and under blowing of argon for various time periods (magenta: 3 min, olive: 6 min, green: 11 min, blue: 16 min, red: 25 min), all under white light irradiation at a power density of 0.3 mW/mm^2 ; (B) photocurrent change (at 10 V) with time upon argon blowing (monitored after 5 min of blowing) and when open to air.

protonation of the amine moiety (Figure S8). Protonation lowers the energy level of the lone electron pair and thus blocks the photoinduced intramolecular electron transfer (Figure S1B), as previously observed for other aniline-modified PTCDI molecules.³³ Both the absorption and excitation spectra measured over the protonated molecules demonstrate the same structural features, particularly in comparison with that measured over molecule **1** (Figure S8). This observation in turn supports the above speculation about the efficient photoinduced intramolecular electron transfer within molecules **3** and **2**.

The only major difference between molecules **2** and **3** lies in the methylene spacer (with one more carbon for **3**) between the aniline moiety and PTCDI. While such a difference results in about 5 times faster intramolecular electron transfer for molecule **2** in comparison to that for **3**,^{48,49} the “too” efficient charge transport mediated by the directly linked D-A also enables rapid charge recombination within the formed geminate electron-hole pairs due to the stronger Coulombic attraction, resulting in loss of free charge carriers that can be transported and collected at the electrodes. In contrast, the increasing of D-A distance in molecule **3** weakens the Coulombic interaction, thus facilitating the separation of the electron-hole pair into free charge carriers. Indeed, under the same measurement conditions, the nanoribbons fabricated from molecule **2** demonstrated negligible photoconductivity, yielding a photocurrent on/off ratio of only ca. 3, which is several orders of magnitude lower than that obtained for the nanoribbons of **3**. This observation implies a way for enhancing the photoconductivity through modification of molecular structure so as to sustain the charge separation state long enough for the subsequent intermolecular charge transport along the long axis of the nanoribbons. Finding a good kinetic balance between these two competitive processes is likely the key to achieve the maximal photoconductivity response.

Effect of Oxygen. All the photoconductivity measurements above were performed under ambient conditions, where the presence of oxygen is expected to result in a decrease in the conductivity due to the strong electron-withdrawing (scavenging) capability, as previously observed for other n-type semiconductor materials in FET performance.²⁰ Considering the large surface area intrinsic to the ultrathin nanoribbons fabricated in this study, the effect of oxygen on the photoconductivity should

be significant, as indeed evidenced in Figure 3. An at least 3 times increase in photocurrent was obtained for the nanoribbons fabricated from molecule **3** when measuring them in a chamber with blowing of argon, in comparison to the measurement under ambient condition. Upon continuous blowing of argon, the photocurrent gradually increased (Figure 3B) until eventually reaching a plateau, indicating the establishment of a surface exchange equilibrium with argon. Upon shutting off the blowing of argon, the photocurrent quickly dropped to a constant value, reflecting the rapid saturation with the adsorption of oxygen. This result is in sharp contrast with the 1D nanostructures fabricated from p-type organic semiconductors, where enhancement of photoconductivity was otherwise observed in the presence of oxygen.¹⁸

The quantum efficiency of the photoconductivity of the nanoribbons under argon can be estimated on the basis of the electrode configuration, the electrical current flowing through the nanoribbons, and the photon flux from the light source.^{9,11} Assuming the average wavelength of white light as 550 nm, a light power of 0.3 mW/mm^2 gives a photon flux of $8.3 \times 10^{20} \text{ photons m}^{-2} \text{ s}^{-1}$. The electrons running through the nanoribbons per second can be calculated as $2.2 \times 10^{10} \text{ electrons s}^{-1}$ (based on 3.6 nA at 15 V). Then the number of electrons transported per photon can be estimated as 63%, which is significantly higher than those previously reported on the other 1D nanomaterials.^{9,11}

As an intrinsic effect of the n-type semiconductor, the same effect of oxygen was also observed for the nanoribbons fabricated from molecule **1**, as depicted in Figure 4. Whereas the conductivity of this nanoribbon is essentially low due to the lack of photogeneration of charge carriers (electrons) as discussed above, almost the same degree of photocurrent modulation (3 times enhanced) was obtained, as compared to the measurement performed over the nanoribbons of **3** (Figure 3). The same degree of modulation of conductivity implies a similar surface access to oxygen, which in turn is consistent with a similar surface area, morphology, and size as observed for the nanoribbons fabricated from the three molecules (Figure 1). Moreover, the negligible photoconductivity observed for the nanoribbons of **1** under both ambient and argon protection clearly indicates that the photogeneration of charge carriers (or photoinduced doping) through the intramolecular charge separation between the D and A moiety is the primary cause for the high photoconductivity observed above for the nanoribbons fabricated from molecule **3**. The high photoconductivity

(48) Adams, D. M.; et al. *J. Phys. Chem. B* **2003**, *107*, 6668–6697.

(49) Xu, B. Q.; Tao, N. J. *Science* **2003**, *301*, 1221–1223.

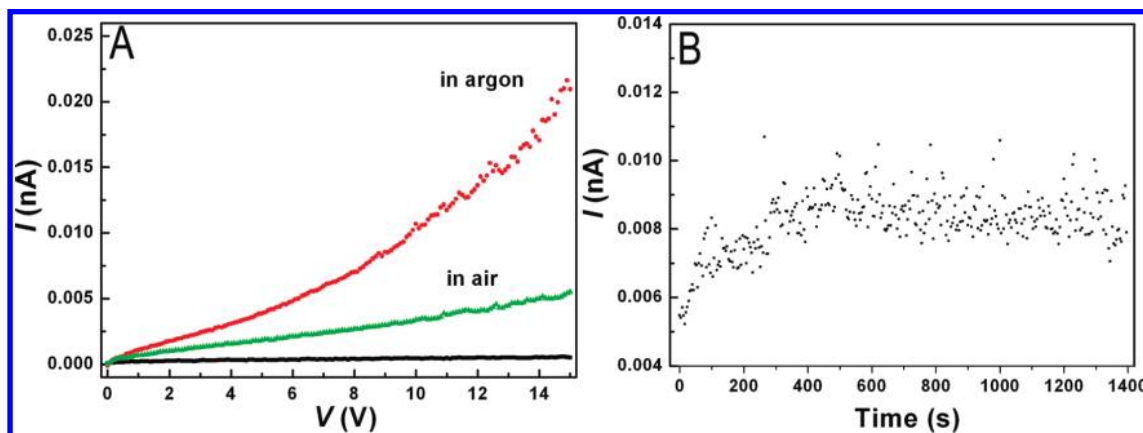


Figure 4. (A) I - V curves measured over the nanoribbons of **1** in air without light irradiation (black), in air (green), and under blowing of argon (red) upon irradiation of white light with a power density of 0.3 mW/mm²; (B) photocurrent change (at 10 V) with time under argon blowing.

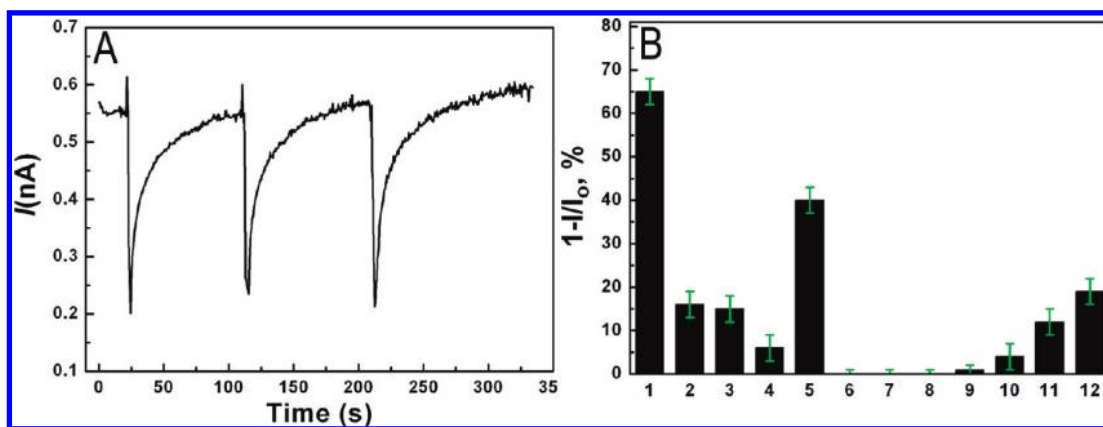


Figure 5. (A) Photocurrent measured over the nanoribbons fabricated from molecule **3** in response to the open-air blowing of saturated vapor of nitromethane; (B) photocurrent response of nanoribbons of molecule **3** to explosive vapors and other organic vapor: (1) nitromethane, 36 000 ppm; (2) nitrobenzene, 150 ppm; (3) 4-nitrotoluene, 100 ppm; (4) 1-chloro-4-nitrobenzene, 15 ppm; (5) 2,4-dinitrotoluene, 0.1 ppm; (6) aniline, 900 ppm; (7) ethanol, 89 000 ppm; (8) acetone, 260 000 ppm; (9) acetonitrile, 100 000 ppm; (10) hexane, 130 000 ppm; (11) toluene, 26 000 ppm; (12) chloroform, 140 000 ppm. The error bar (3%) is also shown.

obtained for the nanoribbons of molecule **3** facilitates the sensing application in vapor detection of explosives as evidenced below.

Sensing Response to Nitro-Based Explosives. Upon deposition onto a substrate, the entangled nanoribbons form a mesh-like, highly porous film (Figure S9), which can provide maximal adsorption and expedient diffusion and accumulation of the gaseous molecules throughout the film matrix.^{39,50–52} Combination of these properties enables efficient vapor sensing of nitro-based explosives, which function the same as oxygen as electron-withdrawing species when adsorbed onto the nanoribbon. Several nitro-based explosives of varying vapor pressures (tens of thousands to tens of ppm), including nitromethane, nitrobenzene, 4-nitrotoluene, and 1-chloro-4-nitrobenzene, were employed herein to prove the concept of the electrical vapor sensing that relies on the photocurrent modulation and takes advantage of the enhanced gas adsorption intrinsic to the porous nanofibril film. The sensing results are presented in Figure 5. We chose these explosive reagents mainly because of their

commercial availability in large amounts and technical ease of vapor handling, for which the high vapor pressure makes them easily introduced into the device simply by blowing with a syringe. The sensing test was also performed for the explosives of low saturated vapor pressure, e.g., 4,6-dinitrotoluene (DNT, 100 ppb at 20 °C).⁵³ Instead of blowing with a syringe, the test was carried out by monitoring the photocurrent change before and after exposing the nanoribbons to the saturated vapor of DNT for 1 min. Figure 5A shows a typical photocurrent response measured over the nanoribbons upon exposure to the vapor of nitromethane, where a sharp decrease in current, by as large as 65%, was observed upon blowing the saturated vapor of nitromethane over the sample. The nanoribbons also exhibited excellent reversibility in the sensing with a quick recovery of the original photocurrent upon stopping the blowing of nitromethane. The quick recovery thus observed is likely due to the volatility intrinsic to nitromethane. For the electrical sensing as depicted here, the quick recovery may facilitate the application in security check points, where constant monitoring of explosives threats is usually demanded.⁵⁴ The efficient electrical response observed for the nitromethane vapor (Figure 5A) is

(50) Naddo, T.; Che, Y.; Zhang, W.; Balakrishnan, K.; Yang, X.; Yen, M.; Zhao, J.; Moore, J. S.; Zang, L. *J. Am. Chem. Soc.* **2007**, *129*, 6978–6979.

(51) Che, Y.; Zang, L. *Chem. Commun.* **2009**, 5106–5108.

(52) Naddo, T.; Yang, X.; Moore, J. S.; Zang, L. *Sens. Actuators, B* **2008**, *B134*, 287–291.

(53) Yang, J.-S.; Swager, T. M. *J. Am. Chem. Soc.* **1998**, *120*, 11864–11873.

(54) DHS Science & Technology Directorate Explosives Division: http://www.dhs.gov/xabout/structure/gc_1224522488810.shtm.

apparently due to the electron affinity of nitromethane, which causes depletion of the charge carriers upon adsorption onto the nanoribbons in the same manner as observed above for oxygen. Although the electron affinity of nitromethane may not be strong enough to cause complete electron withdrawing (charge separation) from the nanoribbon, a partial decrease in the charge density will still be sufficient to be detected by the electrical current measurement. Such electrical-modulation-based sensing is reminiscent of the chemiresistors and chemical-field-effect transistors that have been extensively used in various chemical sensors.^{30,31} A similar efficient photocurrent response was also observed for other explosives vapor as presented and compared in Figure 5B. These results indicate the potential application of the photoconductive nanoribbons in the vapor detection of nitro-based explosives, including those of low vapor pressure.

The electrical sensing described above for the nanoribbons was also performed against the vapor of common organic solvents and some reductive reagents such as aniline, aiming to examine the sensing selectivity. Most of the reference reagents demonstrated negligible current response compared to the target explosives, particularly if considering that the vapor pressures of the former is orders-of-magnitude higher (Figure 5B). Some significant current modulation was observed for organic liquids such as hexane, toluene, and chloroform. We speculate such interference is likely due to the good solubility of PTCDI molecules in these solvents. Vapor condensation of these highly volatile solvents onto the nanoribbon surface may cause a temporary disturbance of the intermolecular arrangement within the nanoribbons (particularly considering the thickness of only ca. 5 nm) and consequently a decrease in conductivity. Upon removal of the solvent vapor (i.e., re-equilibrium with open air), the photocurrent of the nanoribbons can usually be restored instantly. Nonetheless, the sensing selectivity against these solvents as depicted in Figure 5B is still reasonable if considering the fact that the vapor pressures of the solvents employed are thousands of times higher than that of the explosives.

In conclusion, we have successfully fabricated well-defined ultrathin nanoribbons from an amphiphilic D/A molecule. These nanoribbons demonstrated high photoconductivity upon illumination with white light. The high photoconductivity thus obtained is likely due to the optimal molecular design that enables a good kinetic balance between the two competitive processes, the intramolecular charge recombination (between D and A) and the intermolecular charge transport along the nanoribbon. The photogenerated electrons within the nanoribbon can be efficiently trapped by the adsorbed oxygen molecules or other oxidizing species, leading to depletion of the charge carriers (and thus the electrical conductivity) of the nanoribbon. A combination of this sensitive conductivity modulation with the unique features intrinsic to the nanofibril film (large surface area, continuous nanoporosity) enables efficient vapor sensing of nitro-based explosives.

Experimental Section

Synthesis. Molecules **1–3** (Chart 1) were synthesized following the previous methods developed in our and others' laboratories^{34,55} Typically, 200 mg of perylene tetracarboxylic dianhydride and 1 g of dodecyl amine were mixed in 30 mL of ethanol and refluxed for 7 h. The reaction mixture was cooled to room temperature and acidified by 20 mL of concentrated HCl. After stirring overnight,

the resulting red solid was collected by vacuum filtration through a 0.45 μ m membrane filter (Osmonics). The solid was washed thoroughly with methanol and then with distilled water until the pH of the washings turned neutral. The collected solid was then dried under vacuum at 60 °C. The product thus obtained consisted of two compound, perylene tetracarboxylic monoimide and perylene tetracarboxylic diimide, as confirmed by MALDI-MS (m/z = 559 and 726, respectively). This raw product was not further purified before using for the next step of synthesis of the target molecules.

The raw product obtained above (50 mg), 100 mg of the corresponding amine of the functional moiety of molecules **1–3**, and 5 g of imidazole were heated under argon at 120 °C for 3 h. The reaction mixture was cooled to room temperature and dispersed in 25 mL of ethanol, followed by addition of 20 mL of concentrated HCl. After overnight stirring, the resulting red solid was collected by vacuum filtration through a 0.45 μ m membrane filter (Osmonics). The solid was washed thoroughly first with methanol and then with distilled water until the pH of washings turned neutral. The pure compounds of **1–3** were obtained through running column chromatography on a silica gel column, for which chloroform was used as eluent. The pure target compounds as obtained were confirmed by NMR as below.

Compound 1: ¹H NMR (CDCl₃): δ 0.89 (t, 3H, CH₃), 1.17–1.45 (m, 18H, 9CH₂), 1.79 (m, 2H, CH₂), 3.89 (s, 3H, CH₃), 4.21 (m, 2H, CH₂), 7.10 (d, 2H, phenyl), 7.29 (d, 2H, phenyl), 8.69 (m, 8H, perylene). MALDI-MS: m/z = 664.2.

Compound 2: ¹H NMR (CDCl₃): δ 0.86 (t, 3H, CH₃), 1.2–1.4 (m, 18H, 9CH₂), 1.75 (m, 2H, CH₂), 3.12 (s, 6H, 2CH₃), 4.12 (m, 2H, CH₂), 6.87 (d, 2H, phenyl), 7.22 (d, 2H, phenyl), 8.67 (m, 8H, perylene). MALDI-MS: $m+H^+/z$ = 678.3.

Compound 3: ¹H NMR (CDCl₃): δ 0.85 (t, 3H, CH₃), 1.2–1.4 (m, 18H, 9CH₂), 1.78 (m, 2H, CH₂), 2.93 (s, 6H, 2CH₃), 4.24 (m, 2H, CH₂), 5.34 (s, 2H, CH₂), 6.70 (d, 2H, phenyl), 7.54 (d, 2H, phenyl), 8.64 (m, 8H, perylene). MALDI-MS: $m+H^+/z$ = 692.4.

Fabrication of Nanoribbons. All nanoribbons were fabricated by injecting 0.5 mL of a chloroform solution of the compound (0.15 mM) into 2.5 mL of ethanol in a test tube followed by 5 h of aging. The nanoribbons thus formed can be transferred and cast onto a glass surface by pipetting. For molecules **2** and **3**, the fabrication was carried out in the dark (e.g., in the refrigerator) to avoid photooxidation of the aniline part (caused by photoinduced electron transfer).

Structural and Property Characterizations. UV–vis absorption spectra were measured on a PerkinElmer Lambda 25 spectrophotometer. IR spectral measurement was performed on a TENSOR 7 FTIR spectrometer (Bruker). The bright-field optical and fluorescence microscopy imaging was carried out with a Leica DMI4000B inverted microscope, using a Rhodamine filter pak, which provides excitation in the range 530–560 nm and collects emission at >580 nm. SEM measurement was performed with a FEI NanoNova 6300 microscope, and the samples were directly drop-cast on a silica substrate. The FEI NanoNova is a high-resolution SEM allowing for direct imaging of nonconducting materials with feature size down to 2 nm. AFM measurement was performed in tapping mode on a Veeco MultiMode V scanning probe microscope, for which the samples were prepared by spin-casting the nanoribbons dispersed in ethanol on the surface of silica. X-ray diffraction was carried out with a Philips X'Pert XRD instrument.

Photocurrent and Vapor Sensing Measurements. Electrical current measurements of the nanoribbons were carried out through a two-probe method using a Signatone S-1160 probe station, equipped with a Motic microscope for poisoning and a CCD camera for in situ imaging of the device. The probe station is combined with an Agilent 4156C Precision semiconductor parameter analyzer for high-resolution current measurement, and the whole system is housed in a shielding dark box to eliminate the rf noise and/or scattering light for low-current and/or light-sensitive measurements. The microgap electrodes were fabricated by photolithography on a

(55) Che, Y.; Datar, A.; Yang, X.; Naddo, T.; Zhao, J.; Zang, L. *J. Am. Chem. Soc.* **2007**, *129*, 6354–6355.

silicon wafer covered with a 300 nm thick SiO₂ dielectric layer. The gold electrode pair is 14 μ m long and 3 μ m wide, onto which appropriate amounts of nanoribbons were deposited by drop-casting, followed by air-drying in the dark. A tungsten lamp (Quartzline, 21 V, 150 W) was used as the white light source, and the light is guided into the probe station through a glass optical fiber, followed by focusing on the sample through the objective lens. The light power reaching the sample surface was measured by a photon detector. The photocurrent measurements under argon were performed in a homemade chamber that houses the sample in a small gastight system. The vapor sensing measurements were carried out by introducing the saturated vapor of the explosives directly onto the nanoribbons by a syringe. The saturated vapor of DNT was obtained by sealing a small amount of DNT powder in a 50 mL

jar, in which some cotton was used to cover the explosive powder to maintain constant vapor pressure.

Acknowledgment. This work was supported by NSF (CAREER CHE 0641353, CBET 730667), NSFC (20537010), ACS-PRF (45732-G10), and USTAR Program. The work was also supported by the U.S. Department of Homeland Security under cooperative agreement number 2009-ST-108-LR0005.

Supporting Information Available: DFT calculations, spectroscopy, and more optical/electrical microscopy measurements; complete ref 48. This material is available free of charge via the Internet at <http://pubs.acs.org>.

JA909797Q